Journal of ELECTRONIC MATERIALS, Vol. 46, No. 11, 2017
DOI: 10.1007/s11664-017-5634-2

Study on the Effect of Mn, Zn, and Sb on Undercooling Behavior of Sn-Ag-Cu Alloys Using Differential Thermal Analysis

JIE MAO,[1] BENJAMIN REEVES,[1] BRENDAN LENZ,[1]
DANIEL RUSCITTO,[1] and DAN LEWIS[1,2]

1.—Rensselaer Polytechnic Institute, Troy, NY 12180, USA. 2.—e-mail: lewisd2@rpi.edu

Differential thermal analysis (DTA) has been conducted on directionally solidified near-eutectic Sn-3.0 wt.%Ag-0.5 wt.%Cu (SAC), SAC + 0.2 wt.%Sb, SAC + 0.2 wt.%Mn, and SAC + 0.2 wt.%Zn. Laser ablation inductively coupled plasma mass spectroscopy was used to study element partitioning behavior and estimate DTA sample compositions. Mn and Zn additives reduced the undercooling of SAC from 20.4°C to 4.9°C and 2°C, respectively. Measurements were performed at cooling rate of 10°C per minute. After introducing 200 ppm O_2 into the DTA, this undercooling reduction ceased for SAC + Mn but persisted for SAC + Zn.

Key words: Solder, nucleation, lead-free

INTRODUCTION

Sn-Ag-Cu (SAC) alloys are considered to be some of the best lead-free solders, and are being adopted in the microelectronics packaging industry.[1] The eutectic structure is composed of a β-Sn matrix and two intermetallic compounds (IMCs), Cu_6Sn_5 and Ag_3Sn.[2] Experiments and CALPHAD-based computations have established eutectic compositions and temperatures of Sn-3.5%Ag-0.9%Cu at 217°C and Sn-3.7%Ag-0.9%Cu at 217°C.[3,4] Because SAC is composed mainly of Sn, the behavior of Sn determines the final properties of the solder. Other authors[5–8] observed large undercooling in Sn and Sn-rich alloys: these data may result from a large energy barrier for nucleation,[9] because liquid Sn retains some covalent character and organizes adjacent atoms into fragments of tetrahedrally coordinated structures,[10–12] which is very different from the body-centered tetragonal (BCT) structure of β-Sn.

Solder bumps act as electrical, mechanical, and thermal connections. After the first nucleation event for β-Sn, it is hypothesized that the combination of large undercooling (ΔT), high solidification velocity, and recalescence suppresses growth of other nuclei, coarsening the final solder bump grain structure.[13,14] This coarse structure,[4,15–17] coupled with the highly anisotropic mechanical properties of β-Sn,[18–24] leads to high variance in properties between solder bumps. Solder bumps with dominant Sn grains tend to crack when the *c*-axis of the Sn grain is parallel to the substrate, which is attributable to the higher coefficient of thermal expansion (CTE) and shear modulus along the *c*-axis relative to the *a*-axis.[15] Conversely, electromigration (EM) failure in solder joints occurs faster when the *c*-axis of dominant Sn grains is perpendicular to the substrate.[25] As wafer diameters increase, the concomitant rise in the number of solder bumps increases the likelihood of a solder bump with unfavorable final microstructure.[17] Grain refinement of solder bumps can result in larger numbers of randomly oriented crystal grains, thus improving the balance between mechanical and EM performance; For example, Lee et al. studied the link between microstructure and EM and found that reducing the grain size reduces EM failures.[26]

One possible strategy for refining grain structure is through reduction of ΔT. In previous experiments, Mn, Zn, Ti, Ni, Fe, Al, Sb, and Co additives lowered the ΔT of SAC and other Sn-rich solder systems.[27–30] Furthermore, ΔT reduction in the nucleation of Au was observed and attributed to

---

(Received December 18, 2015; accepted June 2, 2017;

the reaction of impurities with O_2,[31] and Swenson proposed that Zn oxides may be responsible for undercooling reduction in SAC + Zn.[32] Based on these results, this study investigated the effects of elemental additives (Sb, Mn, and Zn) and O_2-containing atmosphere on the nucleation and solidification of SAC. We considered two hypotheses in this study: that alloying additives either nucleate β-Sn by modification of the liquid structure, or result in solid phases (oxides or primary intermetallic phases) which alter the solidification process. Based on previous undercooling studies,[7,28] 0.2 wt.% was chosen as the target additive element concentration in this work.

EXPERIMENTAL PROCEDURES

For directionally solidified (DS) ingots, the base alloy was near-eutectic SAC305 from Alpha (South Plainfield, NJ), and the additives used were 99.999% pure Sb from Sigma-Aldrich Co., 99.99% pure Zn from Cominco American, and 99.98% pure Mn from Alfa Aesar. All reported compositions are given as % by mass. Master alloy preparation and directional solidification (DS) at 100 μm/s were carried out following Schaefer et al. and Allen et al.[33–34] The ingots were approximately 5 mm in diameter and 30 cm in length. The DS furnace set point was 400°C, and the temperature gradient in air between the hot and cold zones was 83°C/cm. For the remaining experimental procedures, we assume that there is no macrosegregation in the transverse direction.

Differential thermal analysis (DTA) was conducted using a Netzsch STA-409CD system calibrated to the melting temperatures of In, Sn, Bi, Al, and Au by extrapolating peak tangents back to baseline. To minimize compositional variations, DTA specimens were cut from DS ingots. Using SiC grinding paper, specimens were ground to 99 ± 1 mg to minimize the influence of sample size and geometry on the DTA results. To minimize specimen contamination, all of the Al_2O_3 crucibles (purchased from Netzsch) were new and preconditioned in the DTA by ramping from room temperature to 800°C at 10°C/min, holding for 30 min, and furnace cooling. Atmospheres consisted of ultra-high-purity (UHP) He or UHP He + 200 ppm O_2 mixture supplied at 90 mL/min. For He + O_2 experiments, specimens were heated and cooled four times in UHP He to establish control data, then 200 ppm O_2 was introduced into the DTA atmosphere by evacuating and purging the DTA sample chamber three times with the target He + O_2 mixture. Every specimen was tested using the following temperature programming: from ambient temperature, the furnace was heated to 300°C at 10°C/min, held for 10 min to ensure complete sample melting and temperature stabilization, cooled at 10°C/min to 100°C, held for 10 min, then cycled at 10°C/min three times between 300°C and 100°C. The peak tangent method[35] was used to determine the onset temperature of each thermal event, and the data collected from the first sample melting experiment were discarded due to variable contact area between the sample and crucible.

Estimation of errors for melting follows National Institute of Standards and Technology (NIST) technical note 1297 entitled "Guidelines for Evaluating and Expressing the Uncertainty of NIST Measurement Results."[36] The melting onset temperatures of pure metals and eutectic morphologies in alloys are fixed values. The uncertainty of measurements is likely caused by the experimental setup and operations. The measured temperatures are assumed to follow a normal distribution. Based on the number of independent measurements (degrees of freedom), a coverage factor (f) can be determined. Definition and examples of applying coverage factors to measurement results can be found in Section 7 of NIST Technical Note 1297.[36] Table B.1[36] was used to determine the coverage factors, and in this work a 95% level of confidence is used when reporting temperatures.

For DTA experiments using oxide particles, 99.9% pure ZnO powder (<5 μm) and 99% pure MnO ($\sim$250 μm) were purchased from Sigma Aldrich. Baselines were established for crucibles containing the metal oxides, then specimens were buried in the powders to maximize contact area. The smaller thermal conductivity and larger heat capacity of the sample crucibles with loosely packed oxide particles caused increased delay between thermal events and thermocouple detection. These delays were estimated by comparing the melting temperature (T_m) of SAC with and without oxide particles. The offset was roughly 2°C, causing the measured ΔT to be around 4°C higher. In "Thermograms and Analysis" section, ΔT_{na} is the ΔT value with this correction applied.

T_m was determined from the onset of the first thermal event during heating and is assumed to be due to melting eutectic structures. The first solidification onset temperature (T_{S1}) and second solidification onset temperature (T_{S2}) are defined as the onset of the first and second thermal events during a cooling cycle, respectively. For clarity, when only one thermal event was observed during solidification, it is referred to as T_{S1}. ΔT was calculated as $\Delta T = T_m - T_{S1}$.

The partitioning of alloying elements was first investigated using light optical microscopy (LOM), followed by scanning electron microscopy (SEM) and energy-dispersive x-ray spectroscopy (EDS) mapping on a JEOL JSM-840 SEM. Some features were later quantified using wavelength-dispersive x-ray spectroscopy (WDS) with a Cameca SX100 electron probe microanalyzer (EPMA). Alloy compositions and elemental partitioning behavior of both native elements and additives were later studied by laser ablation inductively coupled plasma mass spectroscopy (LA-ICPMS). LA-ICPMS analyses were performed at the Corman Center for Mass Spectrometry at Rensselaer Polytechnic Institute using a Bruker 820-MS quadrupole ICP-MS interfaced with a Photon Machines Analyte.193 ArF excimer laser system. Concentrations were determined using NIST SRM-610 glass as external calibration standard and Sn-117 as internal standard.

Post-DTA SAC + Mn specimens were deep-etched using a procedure similar to Jackson's.[37] The post-DTA specimens were mounted in epoxy and ground using 240-grit SiC with paper backing until the alloy was exposed. The specimen was rinsed with ethanol, then treated in solution of 5 ± 1 mL 3 M HCl in 20 ± 1 mL ethanol for 1 h. Next, the specimen was removed from the solution, rinsed with ethanol, and treated in solution of 5 ± 1 mL 69.5% HNO_3 in 20 ± 1 mL reverse-osmosis-purified water for 5 min. The specimen was then removed from this solution, flushed with water, treated again in solution of 5 ± 1 mL 3 M aqueous HCl in 20 ± 1 mL ethanol for 1 h, and flushed with ethanol. Finally, the deep-etched specimen was carbon-coated in preparation for SEM. This etching procedure preferentially removed Sn from the microstructure, allowing larger volumes of the specimen to be scanned for features rather than serialized inspection of single sections, and also eliminated time-intensive metallographic preparation.

RESULTS AND DISCUSSION

Composition Analysis

Parameter Determination for LA-ICPMS Composition Measurement

The DS speed (100 μm/s) chosen in this work is slower than the solidification of a deeply undercooled solder bump, which can potentially cause deviations of morphological features [dendrite and intermetallic compound (IMC) spacings]. However, the controlled growth direction can facilitate investigation of the partitioning and macrosegregation of elements. Slow growth speed can also promote uniform distribution of elements along ingots. To study the partitioning behavior of minor alloying elements (0.2% Sb, Zn, or Sb) and to estimate the chemistry of the DTA specimens, LA-ICPMS was adopted. The major advantages of this technique are its low detection limit when compared with EDS or EPMA and its ability to establish spatial correlation of different elements. The major disadvantage of this technique is the difficulty of bulk analysis, especially for materials with coarse microstructures. The estimation of bulk composition is based on the average of a number of measurements. The minimum number of measurements and the minimum spot size have to be estimated beforehand.

For SAC-based solder alloys, a major cause of inhomogeneity is their pronounced dendritic structure. Ag and Cu are enriched in interdendritic regions, causing deviation of the local composition from the overall composition. Assuming that Ag and Cu have near-zero solubility in β-Sn, and are evenly distributed between dendrites, their measured concentrations equal that of the bulk when the sampling area has the same local dendritic volume ratio (DVR) as the bulk. The probability that the sampled DVR will equal that of the bulk increases as the sampling area is increased. Therefore, fewer spots are needed when larger laser spot sizes are used. However, large spots tend to cause insufficient ionization of the ablated atoms, leading to deviation of atomic ratios. An optimum combination of spot size and number is therefore needed.

This combination was estimated by image analysis of the sample microstructure. Images of transverse sections were acquired by stereomicroscope in oblique lighting condition for improved contrast between dendrite and eutectic morphologies. An image analysis algorithm was developed to randomly select areas in the image and measure the local DVR. The projected area in the image analysis algorithm has the same effective size as the laser spot used in LA-ICPMS. This random sampling and measuring process simulates the LA-ICPMS experiment. If the measured average DVR is close to the bulk DVR, the spot size and number combination can be regarded as able to yield the bulk composition. It was confirmed that the sampled local DVR follows a normal distribution. The influence of laser spot size and sampling volume upon the average and standard deviation of the DVR is shown in Fig. 1.

As shown in Fig. 1a, fewer samples are needed when the spot size is larger. To obtain a reasonable estimation, no fewer than ten measurements should be conducted. Larger spot size tends to yield smaller standard deviation of DVR, as shown in Fig. 1b. When the laser spot is over 80 μm, the advantage of increasing the spot size becomes less prominent. Since all the studied alloys have similar microstructural features (dendrite and interdendritic morphologies), this estimation was assumed to hold for all the DS ingots.

Element Macrosegregation

To ensure that macrosegregation did not contribute to variations in the DTA measurements, three specimens were taken from each DS ingot used in this work. Sections were collected at 50 mm, 95 mm, and 145 mm from the initial solid–liquid interface. If there is no statistically significant measurement of compositional variation along the length of the ingot, then the DTA sample composition will be indistinguishable from the bulk composition. Comparisons were made using a paired *t*-test and 95% confidence interval. With the exception of SAC + Zn, all ingots showed statistically insignificant variations due to macrosegregation. According to Fryer et al.,[38] Zn has higher relative

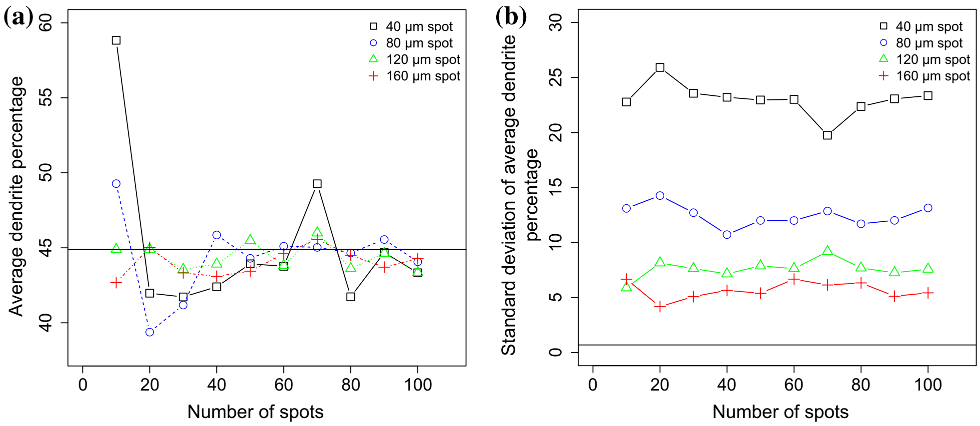

Fig. 1. DVR image analysis results for SAC: effect of spot size and sample size on (a) average estimated DVR, and (b) estimated standard deviation of DVR.

fractionation index in LA-ICPMS than other elements studied using this technique, causing increased uncertainties in the measurement. Development of a special calibration method and standard is needed to confirm the compositional variance of directionally solidified SAC + Zn, which lies beyond the scope of this work. All specimens were taken from the 95-mm position of the DS ingot.

The concentrations of Ag, Cu, and additive elements are plotted against position in the DS ingots in Fig. 2.

DTA Sample Composition

LA-ICPMS measurements using a 120-μm spot size on the ingot specimens are summarized in Table I. The overestimation of the Zn concentration is caused by its higher fractionation index relative to other elements studied.[38] Microstructural inhomogeneity and different ablation responses of elements in SAC and the SRM-610 standard glass contribute to the measured concentration differences. Since no statistically significant elemental macrosegregation of elements was observed and multiple DTA specimens were taken from the 95-mm position of the DS ingots, it is assumed that the entire transverse sample used to fabricate the DTA specimens used in this work was at the target composition.

Differential Thermal Analysis

Effect of DTA Specimen Mass on Composition

The dendrite morphology introduces a deviation of local chemistry compared with the bulk composition. The DTA specimens are small relative to the DS ingots, so the deviation of sampled compositions compared with the bulk has to be estimated. Large DTA sections can better represent the bulk chemistry and yield more consistent results, but large DTA samples are not favored due to time-constant effects in measurements. Since this deviation in composition is dependent on the local DVR in DTA specimens, a similar image analysis approach was used as in “Parameter Determination for LA-ICPMS Composition Measurement” section to study the relationship between local DVR and specimen mass. A 1-cm longitudinal section was taken from the middle part of each DS ingot for analysis. By randomly measuring the local DVR in a stripe with a certain width in the micrograph, which is determined by the sample mass, the variation of DVR can be quantified, as shown in Fig. 3. The averages and standard deviations of DVR for each sample mass are based on 200 randomly selected stripes.

For all the alloys studied in this work, 100 mg was chosen as the target DTA sample mass. Using the target sample compositions (SAC305 + 0.2%X), the estimated concentrations and variations in 100-mg DTA specimens are listed in Table II. LA-ICPMS data (not shown) suggested that Sb was evenly distributed throughout the specimen. The concentration of Sb was not affected by the deviation of local DVR from the bulk. These data also suggested that Mn did not show affinity for either morphology, and therefore the effect of DTA specimen mass on the SAC + Mn specimen composition is estimated to be less than 0.01.

SAC305 is in the Sn corner of the Sn–Ag–Cu ternary phase diagram, and β-Sn is the primary phase. The gradients of the liquidus surface along the Ag and Cu concentration axes are calculated based on the liquidus projection of the phase diagram.[4] The compositional variations of Ag and Cu listed in Table II result in $\leq 0.31°C$ and $\leq 0.15°C$ uncertainties in the liquidus temperature, respectively. As shown in this section, 100-mg DTA specimens are sufficient to represent the bulk composition for the middle sections of DS ingots, but the variation of element concentrations in the eutectic morphology and the rare existence of Ag-Sn or Cu-Sn binary eutectic morphologies can potentially increase the scatter of the sampled compositions.

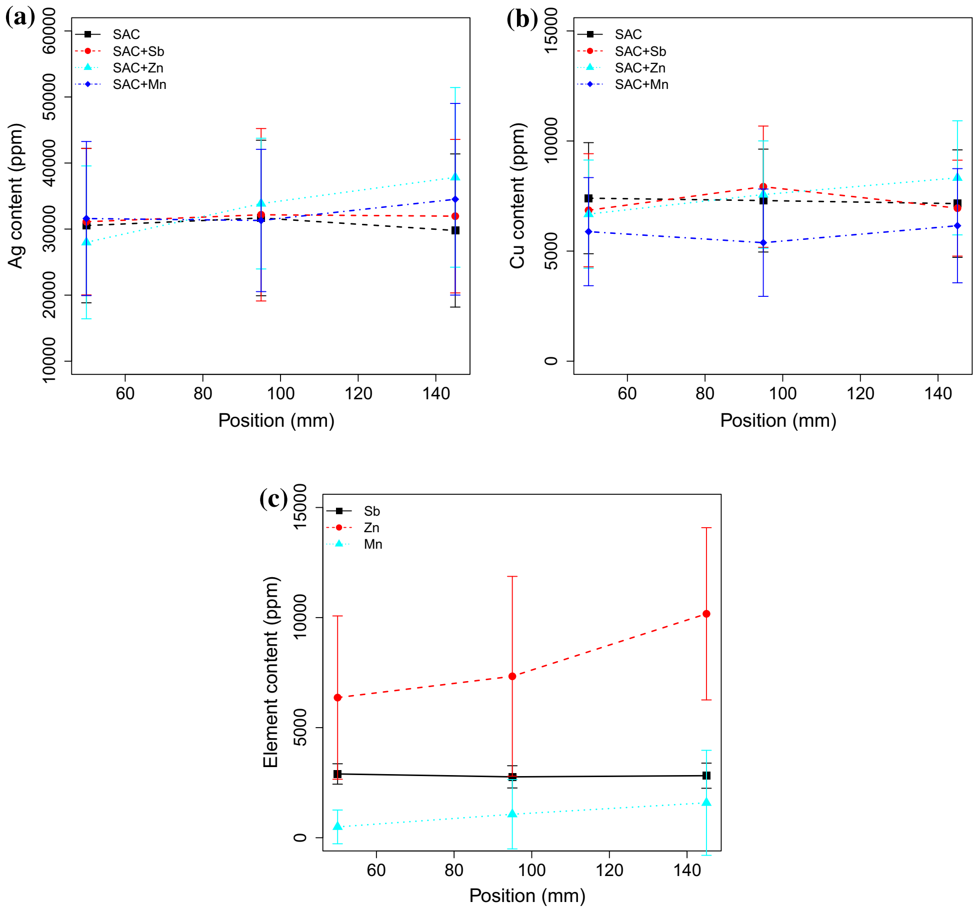

Fig. 2. Alloy element concentration versus ingot position: (a) Ag, (b) Cu, and (c) Sb, Zn, and Mn. Error bars show one standard deviation of measurements.

Table I. Compositions of SAC as reported by the supplier and measured by LA-ICPMS

	Ag (%)	Cu (%)	Sb (%)	Mn (%)	Zn (%)
SAC[39]	3.0 ± 0.2	0.5 ± 0.1	≤ 0.10		≤ 0.001
SAC	3.17 ± 1.18	0.73 ± 0.23			
SAC + Sb	3.22 ± 1.30	0.79 ± 0.28	0.28 ± 0.05		
SAC + Mn	3.13 ± 1.08	0.54 ± 0.27		0.11 ± 0.16	
SAC + Zn	3.39 ± 0.99	0.76 ± 0.24			0.73 ± 0.45

Using 40 measurements, we report the mean and estimate the error as plus or minus one standard deviation. An empty cell indicates that the element was not intentionally added and the concentrations were not measured.

Thermograms and Analysis

A typical DTA thermogram for each alloy is shown in Fig. 4. Exotherms are indicated by positive deviations from the baseline, and endotherms by negative deviations. These figures demonstrate two characteristic behaviors: the low ΔT with a prominent shoulder on the high-temperature side of the exotherm for SAC + Mn and SAC + Zn, and the high ΔT with no shoulder for SAC and SAC + Sb. The average values and standard deviations of T_m, T_{S1}, T_{S2}, and ΔT are presented in Table III. To explain these data, it is important to consider the specimens' morphological characteristics, so representative longitudinal sections are shown in Fig. 5.

To check the performance of the thermal analysis system, T_m of pure Sn was measured multiple times in UHP He following the sample temperature program described in "Experimental Procedures" section. Three specimens tested in this section were prepared in the same way as described in

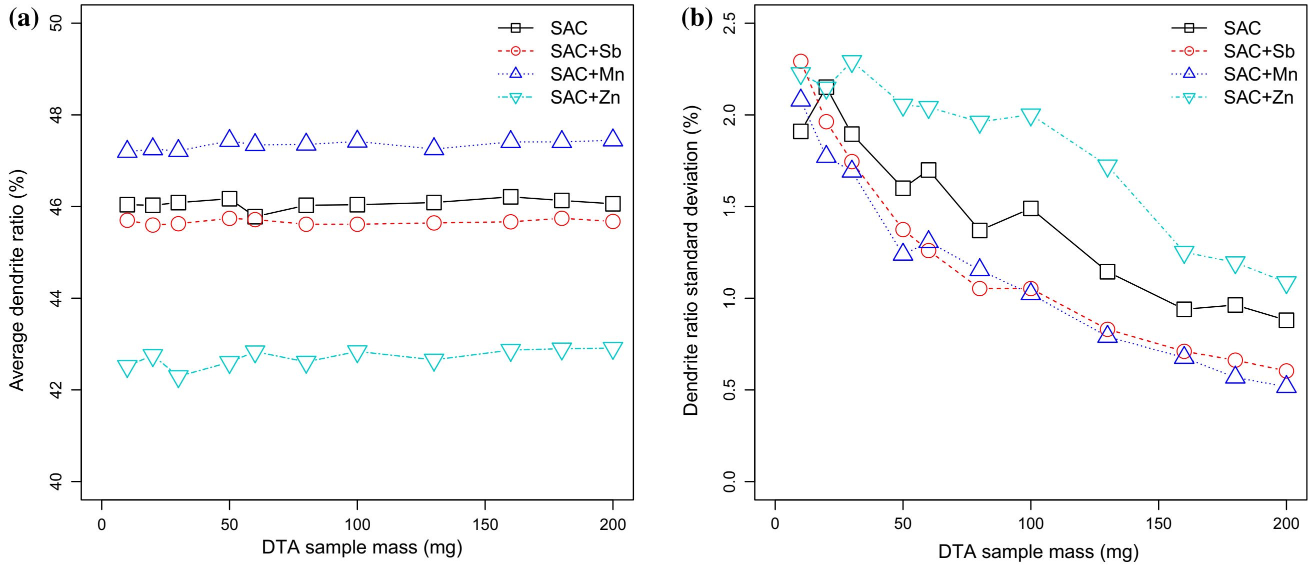

Fig. 3. Effect of DTA sample mass on DVR. (a) Average DVR for choice of sample mass and (b) standard deviation of DVR for choice of sample mass.

Table II. Specified elemental concentrations and estimated standard deviations using 100-mg DTA specimens

	Ag (%)	σ_{Ag} (%)	Cu (%)	σ_{Cu} (%)	Sb (%)	σ_{Sb} (%)	Zn (%)	σ_{Zn} (%)
SAC	3.00	0.08	0.50	0.01				
SAC + Sb	3.00	0.06	0.50	0.01	0.20	0.01		
SAC + Zn	3.00	0.10	0.50	0.02			0.20	0.01

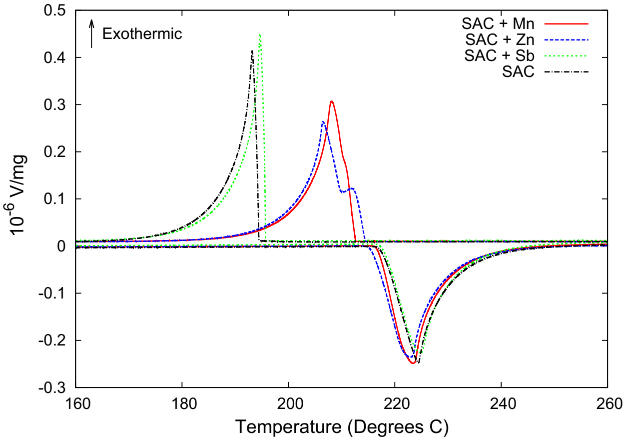

Fig. 4. Thermograms typical of the experiments performed in this work.

“Experimental Procedures” section. The results are listed in Table III.

DTA using UHP He was also performed for three specimens of SAC as control. Referring to Table III, the average SAC ΔT values varied widely between specimens and had large standard deviations. However, since the four runs for each individual specimen (not shown) had narrowly distributed ΔT, the measured variation could be caused by compositional variations between specimens. According to “DTA Sample Composition” section, alloys studied in this work are within the region where β-Sn is the primary phase.[4] The variance of measured undercooling is affected by the liquidus temperature, which is determined by the alloy composition. However, the estimated variances of liquidus temperature shown in “Effect of DTA Specimen Mass on Composition” section are smaller than the observed variances of undercooling listed in Table III. The estimation was conducted assuming coupled growth of Ag- and Cu-enriched phases in the ternary eutectic morphology.

Two SAC specimens were exposed to O_2 during DTA following the procedure described in “Experimental Procedures” section, as control for following experiments. The results are listed in Table IV, and ΔT and T_m for each run are plotted in Fig. 6. T_m stayed the same, while ΔT increased by about 5°C after the introduction of oxygen.

DTA using UHP He was performed for three specimens of SAC + 0.2% Sb, and the results are presented in Table III. Previous studies resulted in undercooling measurements of 5°C for 99.999% pure Sn with Sb addition of 0.1% by mass,[29] but

Table III. Differential thermal analysis results in UHP He

Sample	T_m (°C)	T_{S1} (°C)	T_{S2} (°C)	ΔT (°C)
Sn	232.1 ± 0.3	203.0 ± 5.0		29.0 ± 5.0
SAC	217.9 ± 0.3	197.5 ± 3.7		20.4 ± 3.7
SAC + Sb	218.1 ± 0	195.8 ± 2.2		22.1 ± 2.2
SAC + Mn	217.3 ± 0.6	212.4 ± 0.4	210.9 ± 0.3	4.9 ± 0.4
SAC + Zn	216.4 ± 1.0	214.4 ± 0.2	211.0 ± 0.3	2.0 ± 0.4

See "Experimental Procedures" section for definitions of the different temperatures measured in these experiments. The temperatures are reported as the mean value plus/minus a range corresponding to a 95% confidence interval.

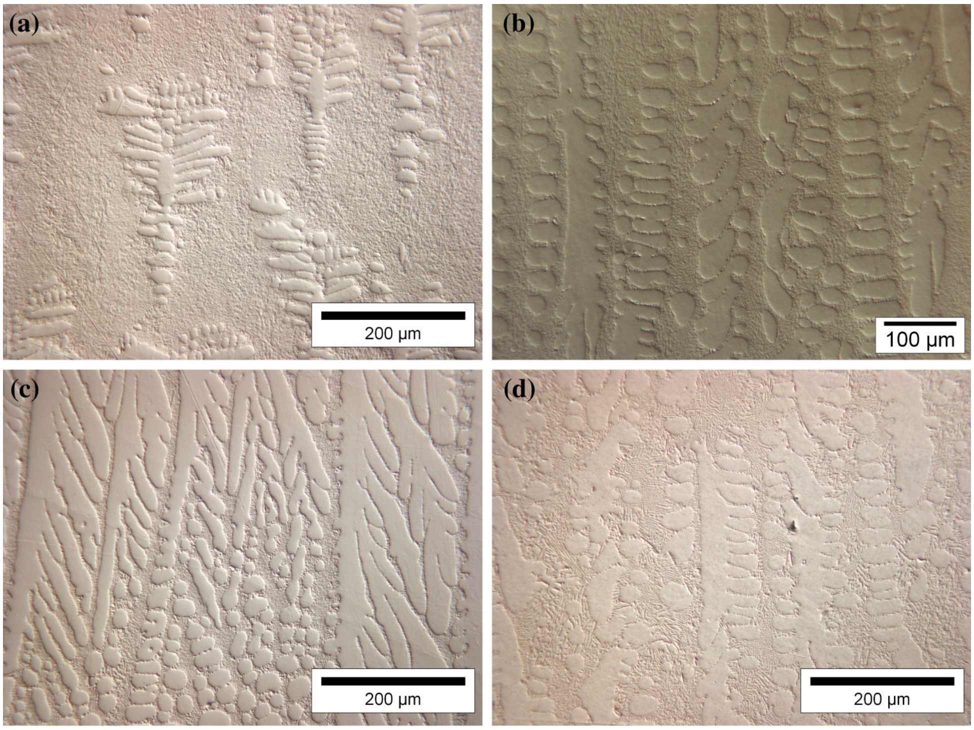

Fig. 5. Longitudinal LOM micrographs of DS specimens solidified at 100 μm/s. Contrasting (a) with (b), (c), and (d) shows the prominent effects apparently caused by the 0.2% Zn, Sb, and Mn additives.

our thermal analysis did not measure a thermal event in this range, indicating that Sb did not reduce the undercooling of β-Sn in the SAC alloy. Our finding is contrary to previous results in literature.

As seen in Fig. 5c, Sb-rich IMC phases were not observed by LOM or SEM, indicating that Sb (at 0.2 wt.%) dissolved in the Sn matrix, in agreement with the phase diagram. LA-ICPMS confirmed Sb's presence and found Sb evenly distributed in the microstructure. While we did not observe lower undercooling, there were marked differences in the microstructure of the specimens containing Sb compared with SAC. Notably, SAC + Sb specimens had continuous dendritic structures, and the primary and side branches appeared to grow at an angle to the imposed thermal gradient.

DTA using UHP He was performed for five specimens of SAC + 0.2%Mn. As seen from the results in Table III, this additive reduced the ΔT and T_m of SAC. Referring to Fig. 5a and d, the β-Sn dendrites for SAC + Mn specimens were more continuous, and the apparent volume fraction of eutectic structure was reduced. Similar structures are seen in Fig. 7 for SAC + Mn alloys directionally solidified at different rates, supporting the observation that the microstructural differences between SAC and SAC + Mn are the result of different growth rates caused by Mn's reduction of ΔT.

As shown in Fig. 4, a common feature of SAC + Mn thermograms is the shoulder at T_{S2} on the high-temperature edge of the exotherm, suggesting one solidification event closely followed by another. The

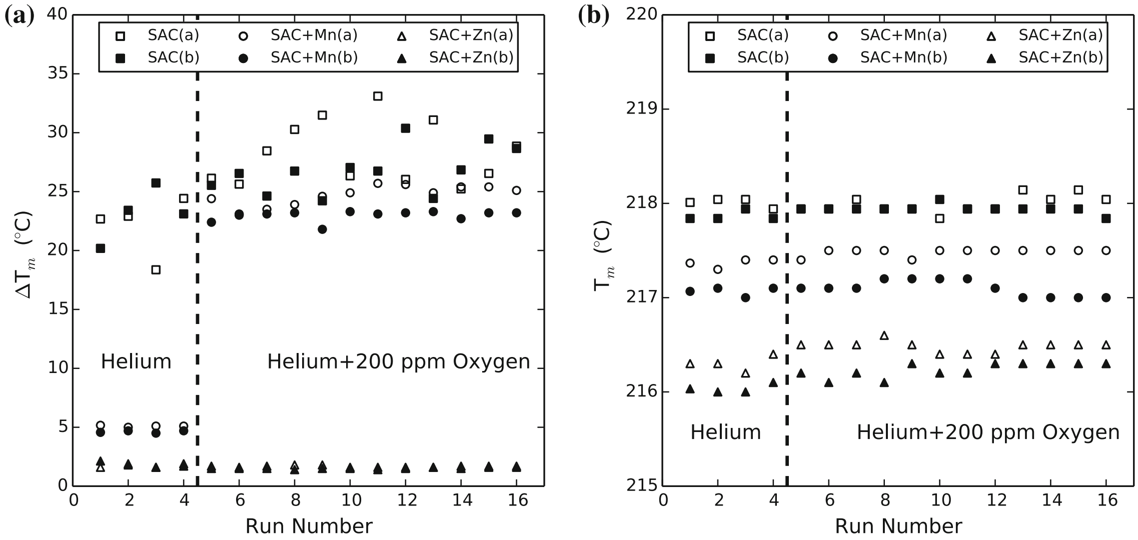

Fig. 6. Plots of melting temperature (a) and undercooling (b) showing the effect of O_2 introduction for SAC, SAC + Zn, and SAC + Mn alloys.

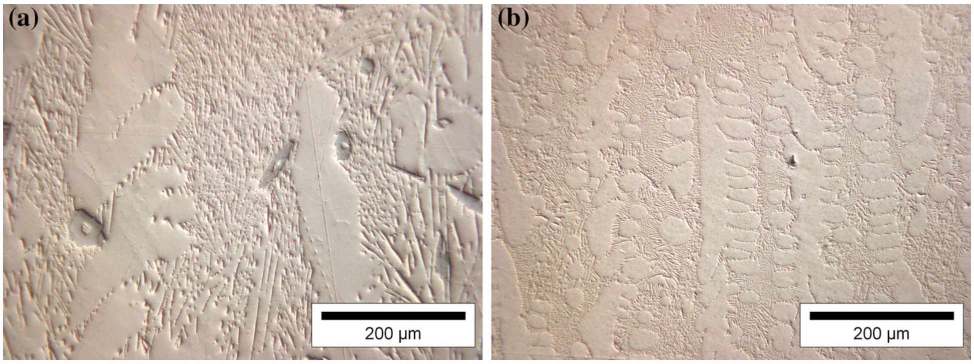

Fig. 7. LOM images of SAC + Mn longitudinal sections directionally solidified at (a) 10 μm/s and (b) 100 μ/s, revealing how microstructures vary with growth rate. Also, because dendrite growth rates are proportional to ΔT, they help explain the microstructures resulting from ΔT-lowering alloying elements such as Zn and Mn.

SEM and EDS results for DS specimens shown in Figs. 8 and 9 reveal "hollow rod" Mn IMC in the microstructure, later confirmed as $MnSn_2$ by EPMA. The orientation of these $MnSn_2$ structures suggests that they formed ahead of the advancing solidification interface whose temperature is between 217°C and 232°C, implying that these phases were present during the SAC + Mn solidification events shown in Fig. 4.

Two SAC + Mn specimens were exposed to O_2 during DTA following the procedure described in "Experimental Procedures" section. The results are listed in Table IV, and ΔT and T_m for each run are plotted in Fig. 6. After introducing O_2 to SAC + Mn specimens, ΔT increased to about the same level as that of SAC. The increase in ΔT reduced the time between the two solidification events that form the shoulder, resulting in a sharp solidification peak similar to the leftmost exotherm seen in Fig. 10b. T_m stayed lower than that of SAC, but a quantitative relationship between T_m and O_2 could not be determined due to measurement system limitations.

To try to observe the transition between low ΔT and high ΔT, O_2 was introduced directly into the UHP He supply of a SAC + Mn specimen without the evacuation and purging process described in "Experimental Procedures" section. Because the O_2 concentration gradually increased to 200 ppm, it took longer to exhaust Mn in the specimen. Figure 10 shows DTA data and thermograms for a typical test. In this case, ΔT gradually increased as the O_2 level rose. As ΔT increased, the shoulder on the cooling edge gradually disappeared and the solidification peak became steeper and higher due to increased recalescence. Surface discoloration caused by oxidation was found on all the DTA specimens that lost ΔT reduction.

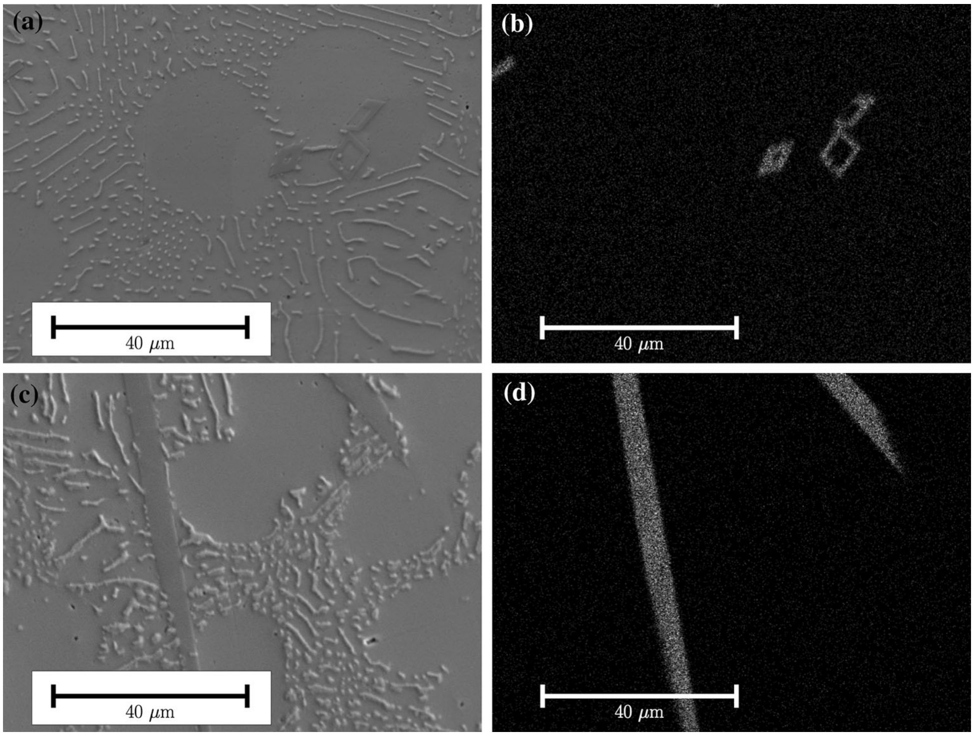

Fig. 8. SEM images and EDS maps of directionally solidified SAC + Mn specimens, showing two views of a hollow-needle Mn phase, later determined to be $MnSn_2$. Panels (a) and (c) show secondary electron images containing intermetallic phases in both hollow rod and long needle morphologies. Panels (b) and (d) show x-ray maps for the Mn k-alpha peak demonstrating that both morphologies belong to the Mn-rich intermetallic phase, $MnSn_2$. Deep etching (see Fig. 9) reveals the full three dimensional morphology of the $MnSn_2$ intermetallic phase.

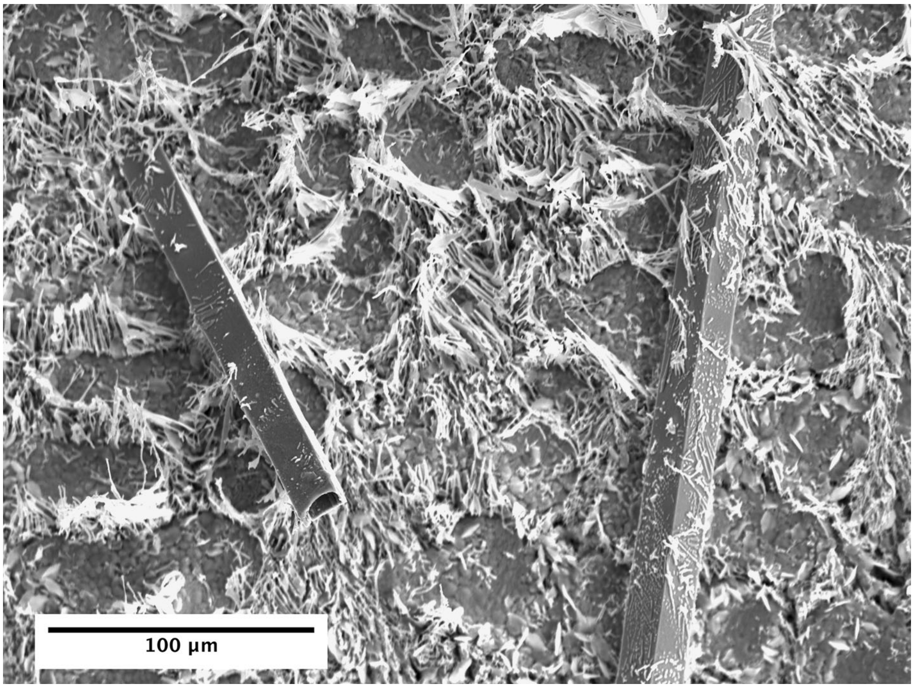

Fig. 9. Secondary electron micrograph of a deep-etched SAC + Mn DTA specimen that retained low ΔT. Mn-containing intermetallic phases are present.

Post-DTA specimens were prepared by standard metallographic procedures and observed using SEM, EDS, and LA-ICPMS. Microstructures before and after O_2 exposure are shown in Fig. 11. In pre-O_2 specimens, i.e., those with low ΔT, $MnSn_2$ IMCs were found dispersed throughout the

Table IV. DTA results for two SAC + Mn and two SAC + Zn specimens, showing the measured T_m and ΔT for both UHP He and UHP He + O_2

	UHP He		He + O_2	
Specimen	**T_m (°C)**	**ΔT (°C)**	**T_m (°C)**	**ΔT (°C)**
SAC	218.0 ± 0	22.1 ± 2.6	218.0 ± 0.3	28.3 ± 2.7
	217.9 ± 0	23.1 ± 2.3	217.9 ± 0	26.8 ± 2.0
SAC + Mn	217.4 ± 0	5.1 ± 0.1	217.5 ± 0	24.7 ± 0.8
	217.1 ± 0	4.6 ± 0.1	217.1 ± 0.3	23.0 ± 0.4
SAC + Zn	216.3 ± 0.3	1.7 ± 0.2	216.5 ± 0	1.7 ± 0.1
	216.0 ± 0	1.8 ± 0.2	216.2 ± 0.3	1.5 ± 0.1

The procedure for DTA and introducing oxygen into the DTA chamber is described in "Experimental Procedures" section.

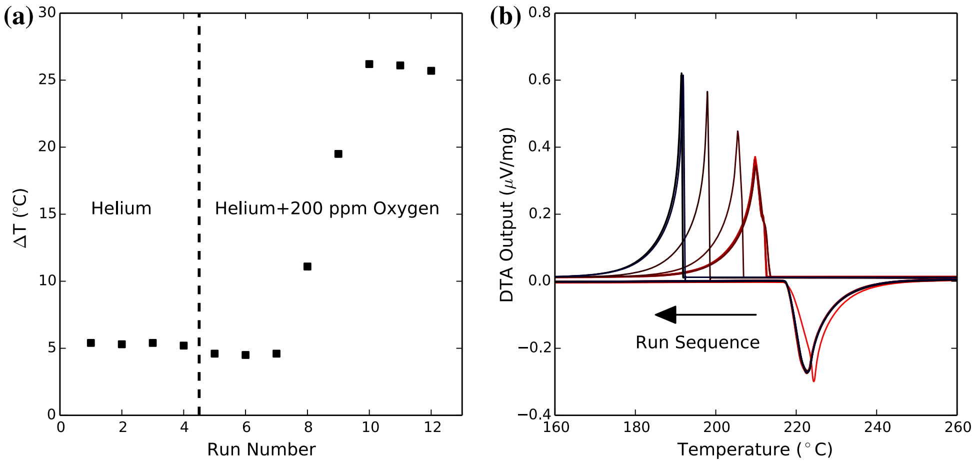

Fig. 10. (a) How ΔT varied during continuous exposure to oxygen in the Mn-containing samples, and (b) the sequence of DTA thermograms obtained during this process.

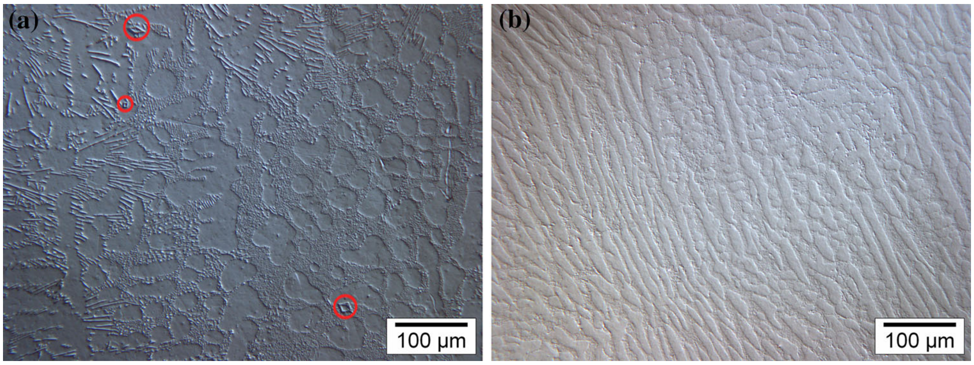

Fig. 11. Post-DTA LOM images of SAC + Mn specimens, showing the differences between (a) a specimen solidified in UHP He and (b) one solidified in UHP He plus oxygen. When low ΔT was observed, $MnSn_2$ phases were also observed. When ΔT stabilized around typical SAC values, no $MnSn_2$ phases were observed.

microstructure, but no $MnSn_2$ IMCs were found in specimens exposed to O_2. However, T_m remained low for both specimens, implying presence of Mn before and after O_2 exposure. To facilitate the search for $MnSn_2$ IMCs in the microstructure, DTA specimens were deep etched following the procedure described in "Experimental Procedures" section. The post-DTA SAC + Mn specimen which was not exposed to O_2 was etched first, then observed by SEM.

The structures in Fig. 9 show that $MnSn_2$ was present after the DTA experiment. The SAC + Mn specimen exposed to O_2 during DTA was then etched following the same procedure. SEM observation after the deep etching procedure did not reveal any $MnSn_2$ IMCs. Because the DS specimens were removed from the same section of the SAC + Mn ingot, and because micrographs show $MnSn_2$ in the specimens which were not studied using DTA, we conclude that $MnSn_2$ IMCs were present in the O_2-free DTA specimen before and after the DTA experiments. These results also justify the use of the etching procedure to search for $MnSn_2$, because they show that $MnSn_2$ endured the etch. The large number of visible $MnSn_2$ IMCs in the first specimen and their absence in the second justifies the positive correlation of $MnSn_2$ with reduced ΔT, but more direct experiments would be necessary to demonstrate causality.

DTA using UHP He was performed on five specimens of SAC + 0.2%Zn, with the results presented in Table III. Zn reduced the ΔT of SAC, which is consistent with previous work by Anderson et al.[7,40] As shown in Fig. 4, Zn resulted in a larger and higher-temperature shoulder on the leading edge of the exotherm. As shown in Fig. 5b, compared with SAC, Zn additive resulted in finer β-Sn dendrites and coarsened the eutectic structure.

Two SAC + Zn specimens were exposed to O_2 during DTA following the procedure described in “Experimental Procedures” section, and the results are shown in Table IV and Fig. 6. The ΔT and T_m stayed low and the exotherm’s shoulder persisted throughout the experiment. Post-DTA specimens were prepared by standard metallographic procedures and analyzed using SEM and LA-ICPMS. No significant microstructural differences were observed using SEM, and the LA-ICPMS data revealed Zn in the microstructure. Surface discoloration due to oxidation was observed on all the post-DTA SAC + Zn specimens that were exposed to O_2. These experiments lend support to the finding by Swenson that ZnO can promote SAC nucleation.[32]

According to the Sn-Ag-Cu liquidus surface projection in Ref. 4, the compositions of the SAC-based alloys used in this work are within the Sn-rich corner, where β-Sn is the primary phase. Since β-Sn is the first phase to precipitate out from the liquid, the reduced undercooling observed above on Mn and Zn addition should be attributed to their promotion of nucleation of β-Sn. Due to small specimen size, fast solidification, and the presence of undercooling, deviation from thermodynamic equilibrium conditions should also be expected. Therefore, the primary phase could also be Ag_3Sn or Cu_6Sn_5, nucleation of which could be promoted by Mn or Zn. If Mn and Zn can also reduce the undercooling of pure Sn, it is very likely that they promoted the nucleation of β-Sn in the SAC alloys. The DTA results for Sn, Sn + 0.2%Mn, and Sn + 0.2%Zn are listed in Table V. The DTA traces are shown in Fig. 12. Since this dataset was collected at 5°C/min, it is listed in this section instead of being included in Table III.

As shown in Table V and Fig. 12, Mn and Zn can also greatly reduce the undercooling of pure Sn. These results suggest that β-Sn is very likely to be the phase that Mn and Zn promoted in SAC alloys studied previously. The common shoulder feature on exotherms of SAC + Mn and SAC + Zn was caused by one solidification event following another. Mn and Zn reduced the nucleation barrier for β-Sn, which caused Sn to precipitate closer to the liquidus temperature, hence the two events on the thermogram: formation of primary β-Sn phase from the liquid, followed by solidification of the remaining phases (β-Sn, Ag_3Sn, and Cu_6Sn_5).

The effect of oxide particles on nucleation promotion and grain refinement has been widely studied, particularly for Al alloys.[41] Some oxides, such as

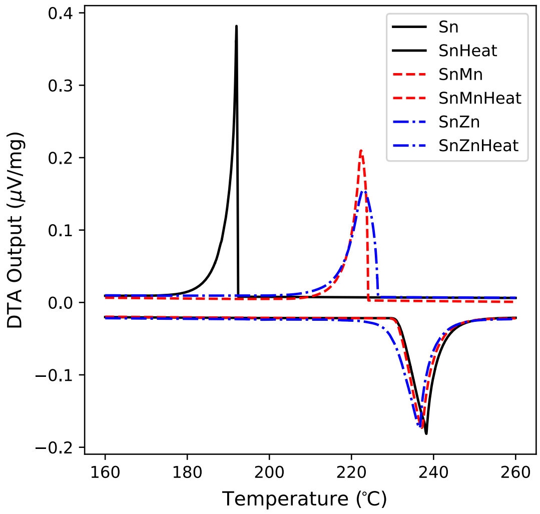

Fig. 12. Typical DTA traces of Sn, Sn + Mn, and Sn + Zn.

Table V. DTA results for Sn, Sn + Mn, and Sn + Zn in He

Sample	T_m (°C)	T_{S1} (°C)	ΔT (°C)
Sn	231.7 ± 0	192.3 ± 0.1	39.4 ± 0.1
Sn + Mn	231.4 ± 0	224.3 ± 0.3	7.1 ± 0.3
Sn + Zn	230.2 ± 0	226.6 ± 0.1	3.6 ± 0.1

TiO_2 and Y_2O_3, have been reported to be effective in refining β-Sn and the eutectic structure.[42,43] As shown in Table VI, Mn and Zn are below Sn, Ag, and Cu on the Ellingham diagram at 300°C, so when exposed to O_2 alongside Sn, Ag, and Cu, these elements are thermodynamically favored to be oxidized. It is possible that formation of these oxides is the reason for these elements' effect on ΔT reduction in solder alloys, particularly for Zn.[32]

The interaction between SAC and metal oxides was investigated using DTA on SAC specimens buried in ZnO and MnO particles, and the T_m, T_{S1}, ΔT, and ΔT_{na} values are presented in Table VII. Comparing these data with those in Table III, the ΔT_{na} values are much higher than the ΔT values for SAC + Mn and SAC + Zn, and the T_m values are larger than those for SAC specimens. Also, there was no shoulder on the exotherms in these thermograms.

While this experiment did not reduce ΔT, it did not rule out ZnO and MnO as nucleation catalysts because the oxidation layers on the specimens might have limited the contact between Sn and ZnO or MnO.

Proposed Undercooling Reduction Mechanisms

Addition of 0.2% Mn effectively reduced the undercooling of SAC. A similar effect has also been observed in Sn + Mn specimens, suggesting that Mn can potentially promote the nucleation of β-Sn phase and reduce the ΔT of both SAC and Sn. After the introduction of O_2 into the carrier gas stream, Mn's undercooling reduction effect disappeared. In the DS microstructure and the post-DTA specimens that retain low ΔT, Mn was found enriched in $MnSn_2$ intermetallic phase. No $MnSn_2$ intermetallic phase was observed in the post-DTA specimen which had lost the undercooling reduction effect, suggesting that $MnSn_2$ is crucial for the nucleation of β-Sn and undercooling reduction. $MnSn_2$ crystallizes in tetragonal $CuAl_2$ structure type ($I4/mcm$), with Mn and Sn atoms occupying 4a and 8h positions, respectively. Dong et al. compared the structure of $MnSn_2$ with the β-Sn structure and found that the (110) plane of the $MnSn_2$ phase matches well with the (100) plane of the β-Sn phase, with distances between the first and second nearest neighboring Sn atoms of 3.034 Å and 3.181 Å for the $MnSn_2$ phase, and 3.022 Å and 3.181 Å for the β-Sn phase; the bond angles do not match as closely.[44] It is possible, then, that the Sn atoms on the (110) plane of $MnSn_2$ served as a substrate for the nucleation of β-Sn. After the introduction of O_2, oxidation reduced the Mn concentration until no $MnSn_2$ phase could precipitate from liquid before the nucleation of β-Sn. This caused the ΔT reduction to almost fully recover typical SAC values. Considering that Mn was present both before and after the loss of undercooling reduction, if Mn addition changed the liquid structure to reduce the energy barrier for nucleation, then one would expect the ΔT reduction to be independent of the presence of $MnSn_2$, which is counter to our experimental results. Therefore, we hypothesize that Mn reduces the ΔT of SAC alloy by formation of the $MnSn_2$ intermetallic phase, which serves as a nucleation substrate for β-Sn and reduces the nucleation barrier.

Zn greatly reduced the ΔT of both SAC and Sn, which suggests that it can promote the nucleation of the β-Sn phase. The ΔT of SAC + Zn DTA specimens was constant under prolonged O_2 exposure, unlike the Mn-doped specimens where the undercooling was eliminated after O_2 exposure. It is likely that ZnO promoted the nucleation of β-Sn and lowered the ΔT of SAC, as proposed by Swenson.[32] Solder alloys buried in ZnO particles failed to reduce the ΔT of SAC during solidification. This could be caused by poor contact between ZnO particles in the DTA specimens and the SAC melt, as discussed in "Thermograms and Analysis" section. This could also mean that ZnO might not be responsible for the undercooling reduction, but rather Zn in solution in liquid Sn may be the controlling mechanism. Unlike most metal elements, which have close-packed icosahedral short-range ordering (ISRO) in the melt, Sn retains some covalent character and

Table VI. Gibbs free energy change for some of the oxidation reactions occurring in SAC + X alloys

Reaction	ΔG (kJ/mol O_2)
$4Cu + O_2 \rightarrow 2Cu_2O$	−254
$4Ag + O_2 \rightarrow 2Ag_2O$	13.3
$2Sn + O_2 \rightarrow 2SnO_2$	−450
$2Mn + O_2 \rightarrow 2MnO_2$	−685
$2Zn + O_2 \rightarrow 2ZnO_2$	−586

These data were calculated using ThermoCalc with the SSUB4 database.

Table VII. DTA experimental results for SAC + MnO and SAC + ZnO, showing T_m, T_{S1}, and ΔT

Sample	T_m (°C)	T_{S1} (°C)	ΔT (°C)	ΔT_{na} (°C)
SAC + MnO	219.7 ± 0	195.4 ± 3.4	24.4 ± 3.4	20.4
SAC + ZnO	219.9 ± 0.2	192.3 ± 1.6	28.0 ± 1.6	24.0

organizes adjacent atoms into fragments of tetrahedrally coordinated structures.[10–12] The difference between this special short-range ordering (SRO) and the BCT structure of β-Sn could be responsible for the high nucleation barrier of Sn and the concomitant high ΔT. According to Refs. 45 and 46, Zn can form icosahedral clusters with Zn enclosed in a 12-coordinated Sn cage and therefore change the SRO of Sn to the more conventional ISRO and facilitate nucleation. Since Zn was found in the microstructure before and after O_2 exposure, it is hard to refute this possibility based on the experiments conducted in this work.

CONCLUSIONS

Addition of 0.2% Mn and Zn reduced the ΔT of near-eutectic SAC. ΔT of Sn was also greatly reduced by 0.2% Mn and Zn addition, suggesting that both Mn and Zn reduced the ΔT of SAC alloy by promoting the nucleation of β-Sn. The DTA exotherms of both SAC + Mn and SAC + Zn exhibited a shoulder at around 211°C, which is caused by the solidification of eutectic microstructure following the solidification of primary β-Sn phase. Addition of 0.2% Sb did not reduce ΔT in near-eutectic SAC. The presence of a quaternary morphology and a reduced T_m relative to SAC would be strong experimental evidence for a quaternary invariant. This study's limitations—notably the large relative uncertainties in T_m of SAC + Mn and SAC + Zn compared with T_m of SAC and the poor spatial resolution of LA-ICPMS—preclude this conclusion, but the results should motivate more thorough investigation of potential quaternary invariant reactions within the SAC + Mn and SAC + Zn systems.

Microstructural analysis of directionally solidified specimens suggested that Mn, Zn, and Sb additives promoted dendrite formation, which tends to introduce local variations of alloy composition. When parts of an ingot are taken for analysis, compositional variation could potentially lead to the ΔT variance commonly seen in literature. High ΔT promotes the formation of dendrites, suppresses the eutectic morphology, and causes the eutectic microstructure to be finer. Sb forms solid solution with Sn and evenly distributes in the microstructure. Mn tends to form $MnSn_2$ intermetallic phases randomly dispersed in the microstructure. No Zn-enriched phase was found via EDS.

O_2 reacts with Mn at elevated temperatures, reducing the Mn concentration to a point where no $MnSn_2$ phase can precipitate from liquid prior to the nucleation of β-Sn. As this occurs, the ΔT reduction disappears. Also, T_m remains low, suggesting that Mn is still present in the liquid. This observation and $MnSn_2$'s structural similarity to β-Sn support our hypothesis that Mn reduces ΔT of SAC by providing $MnSn_2$ as a favorable nucleation substrate for β-Sn.

With Zn addition, ΔT and T_m of the SAC stayed low regardless of oxygen exposure. Zn was detected before and after O_2 exposure, and ZnO was also observed on the specimen surface. Without further experiments, it is difficult to identify the ΔT reduction mechanism of Zn, which could be by either Zn modifying the liquid structure or ZnO acting as a nucleation substrate.

ACKNOWLEDGEMENTS

The authors gratefully acknowledge funding provided by the Semiconductor Research Corporation through The New York Center for Advanced Interconnect Science and Technology research task 1292.089, the IBM Shared University Research Award at Rensselaer, and the Rensselaer Undergraduate Research program. The authors also thank Alpha Metals for donation of the SAC305 alloy used in these experiments.

REFERENCES

1. K. Suganuma, *Curr. Opin. Solid State Mater. Sci.* 5, 55 (2001).
2. D. Lewis, S. Allen, M. Notis, and A. Scotch, *J. Electron. Mater.* 31, 161 (2002).
3. M.E. Loomans and M.E. Fine, *Metall. Mater. Trans. A* 31, 1155 (2000).
4. K.W. Moon, W.J. Boettinger, U.R. Kattner, F.S. Biancaniello, and C.A. Handwerker, *J. Electron. Mater.* 29, 1122 (2000).
5. B. Vonnegut, *J. Colloid Sci.* 3, 563 (1948).
6. K. Kelton, *Solid State Phys.* 45, 75 (1991).
7. I.E. Anderson, J.W. Walleser, J.L. Harringa, F. Laabs, and A. Kracher, *J. Electron. Mater.* 38, 2770 (2009).
8. Y.L. Gao, E. Zhuravlev, C.D. Zou, B. Yang, Q.J. Zhai, and C. Schick, *Acta Thermochim.* 482, 1 (2009).
9. K.F. Kelton and A.K. Gangopadhyay, *Powder Diffr.* 20, 87 (2005).
10. T. Itami, S. Munejiri, T. Masaki, H. Aoki, Y. Ishii, T. Kamiyama, Y. Senda, F. Shimojo, and K. Hoshino, *Phys. Rev. B* 67, 064201 (2003).
11. L. Calderin, D.J. Gonzalez, L.E. Gonzalez, and J.M. Lopez, *J. Chem. Phys.* 129, 194506 (2008).
12. A. Di Cicco, A. Trapananti, E. Principi, S. De Panfilis, and A. Filipponi, *Appl. Phys. Lett.* 89, 221912 (2006).
13. B. Arfaei, N. Kim, and E.J. Cotts, *J. Electron. Mater.* 41, 362 (2012).
14. L.P. Lehman, S.N. Athavale, T.Z. Fullem, A.C. Giamis, R.K. Kinyanjui, M. Lowenstein, K. Mather, R. Patel, D. Rae, J. Wang, Y. Xing, L. Zavalij, P. Borgesen, and E.J. Cotts, *J. Electron. Mater.* 33, 1429 (2004).
15. T.R. Bieler, H. Jiang, L.P. Lehman, T. Kirkpatrick, E.J. Cotts, and B. Nandagopal, *IEEE Trans. Compon. Packag. Technol.* 31, 370 (2008).
16. S.-K. Seo, S.K. Kang, M.G. Cho, D.-Y. Shih, and H.M. Lee, *J. Electron. Mater.* 38, 2461 (2009).
17. J. Sylvestre and A. Blander, *J. Electron. Mater.* 37, 1618 (2008).
18. J.A. Rayne and B. Chandrasekhar, *Phys. Rev.* 120, 1658 (1960).
19. G. Simmons and H. Wang, *Single Crystal Elastic Constants and Calculated Aggregated Properties: A Handbook* (Cambridge: MIT Press, 1971).
20. D.G. House and E.V. Vernon, *Br. J. Appl. Phys.* 11, 254 (1960).
21. H.B. Huntington, *Solid State Phys.* 7, 213 (1958).
22. R.F.S. Hearmon, *Adv. Phys.* 5, 323 (1956).
23. W.P. Mason and H.E. Bommel, *J. Acoust. Soc. Am.* 28, 930 (1956).

24. P.W. Bridgman, *Proc. Natl. Acad. Sci. USA*, 10, 411 (1924).
25. M. Lu, D.-Y. Shih, P. Lauro, C. Goldsmith, and D.W. Henderson, *Appl. Phys. Lett.* 92, 211909 (2008).
26. K. Lee, K.-S. Kim, and K. Suganuma, *J. Mater. Res.* 26, 2624 (2011).
27. J. Song, C. Huang, and H. Chuang, *J. Electron. Mater.* 35, 2154 (2006).
28. I.E. Anderson, J. Walleser, and J.L. Harringa, *J. Mater.* 59, 38 (2007).
29. T. Motegi and A. Ohno, *J. Jpn. Inst. Met.* 37, 777 (1973).
30. D.C. Lin, T.S. Srivatsan, G. Wang, and R. Kovacevic, *Powder Technol.* 166, 38 (2006).
31. G. Wilde, J.L. Sebright, and J.H. Perepezko, *Acta Mater.* 54, 4759 (2006).
32. D. Swenson, *J. Mater. Sci. Mater. Electron.* 18, 39 (2007).
33. R.J. Schaefer and D. J. Lewis, *Met. Mater. Trans. A* 36A, 2775 (2005).
34. S.L. Allen, M.R. Notis, R.R. Chromik, R.P. Vinci, D.J. Lewis, and R. Schaefer, *J. Mater. Res.* 19, 1425 (2004).
35. D. Lewis, M. Notis, and A. Grusd, *J. Phase Equilib.* 21, 425 (2000).
36. B.N. Taylor and C.E. Kuyatt, *NIST Technical Note 1297* (National Institute of Standards and Technology, USA, 1994).
37. I.E. Jackson, *Metallography* 14, 107 (1981).
38. B.J. Fryer, S.E. Jackson, and H.P. Longerich, *Can. Mineral.* 33, 303 (1995).
39. Alpha. Alpha® Vaculoy SAC300,305,350,400,405 lead free wave solder alloy. Technical report, South Plainfield, NJ (2010).
40. I.E. Anderson, A. Boesenberg, J. Harringa, D. Riegner, A. Steinmetz, and D. Hillman, *J. Electron. Mater.* 41, 390 (2012).
41. H.T. Li, Y. Wang, and Y. Fan, *Acta Mater.* 60, 1528 (2012).
42. L.C. Tsao and S.Y. Chang, *Mater. Des.* 31, 990 (2010).
43. X. Liu, M. Huang, C.M.L. Wu, and L. Wang, *J. Mater. Sci. Mater. Electron.* 21, 1046 (2010).
44. Y. Dong and F. DiSalvo, *Acta Crystallogr. E* 61, 282 (2005).
45. B.T. Truong, M.T. Nguyen, and M.T. Nguyen, *Chem. Phys.* 388, 1 (2011).
46. S. Neukermans, X. Wang, N. Veldeman, E. Janssens, R.E. Silverans, and P. Lievens, *Int. J. Mass Spectrom.* 252, 145 (2006).